The Astrophysical Journal Letters, 943:L21 (7pp), 2023 February 1 https://doi.org/10.3847/2041-8213/acb260

Saturation of the Filamentation Instability and Dispersion Measure of Fast Radio Bursts

Emanuele Sobacchi[1,2], Yuri Lyubarsky[3], Andrei M. Beloborodov[4,5], Lorenzo Sironi[1], and Masanori Iwamoto[6]
[1] Department of Astronomy and Columbia Astrophysics Laboratory, Columbia University, New York, NY 10027, USA; emanuele.sobacchi@mail.huji.ac.il
[2] Racah Institute for Physics, The Hebrew University, Jerusalem 91904, Israel
[3] Physics Department, Ben-Gurion University, P.O.B. 653, Beer-Sheva 84105, Israel
[4] Physics Department and Columbia Astrophysics Laboratory, Columbia University, 538 West 120th Street, New York, NY 10027, USA
[5] Max Planck Institute for Astrophysics, Karl-Schwarzschild-Str. 1, D-85741, Garching, Germany
[6] Faculty of Engineering Sciences, Kyushu University, 6-1, Kasuga-koen, Kasuga, Fukuoka, 816-8580, Japan
Received 2022 October 8; revised 2023 January 11; accepted 2023 January 12; published 2023 February 1

Abstract

Nonlinear effects are crucial for the propagation of fast radio bursts (FRBs) near the source. We study the filamentation of FRBs in the relativistic winds of magnetars, which are commonly invoked as the most natural FRB progenitors. As a result of filamentation, the particle number density and radiation intensity develop strong gradients along the direction of the wind magnetic field. A steady state is reached when the plasma pressure balances the ponderomotive force. In such a steady state, particles are confined in periodically spaced thin sheets, and electromagnetic waves propagate between them as in a waveguide. We show the following. (i) The dispersion relation resembles that in the initial homogeneous plasma, but the effective plasma frequency is determined by the separation of the sheets, not directly by the mean particle density. (ii) The contribution of relativistic magnetar winds to the dispersion measure of FRBs could be several orders of magnitude larger than previously thought. The dispersion measure of the wind depends on the properties of individual bursts (e.g., the luminosity) and therefore can change significantly among different bursts from repeating FRBs. (iii) Induced Compton scattering is suppressed because most of the radiation propagates in near-vacuum regions.

Unified Astronomy Thesaurus concepts: Radio transient sources (2008); Plasma astrophysics (1261)

1. Introduction

Fast radio bursts (FRBs) are bright flashes of millisecond duration likely produced by magnetars (e.g., Cordes & Chatterjee 2019; Petroff et al. 2019, 2022). Since, near the source, the electromagnetic field of the radio wave accelerates the electrons up to a significant fraction of the speed of light, nonlinear effects are crucial for the propagation of FRBs (e.g., Lyubarsky 2021).

In our previous work (Sobacchi et al. 2022), we studied the filamentation of FRBs in magnetar winds.[7] We showed that the radiation intensity and particle density develop spatial modulations along the direction of the wind magnetic field. However, since we focused on the linear stability analysis of the filamentation instability, we could not predict what happens after the initial phase of exponential growth.

In this paper, we present a model for the saturation of the filamentation instability of FRBs in magnetar winds. Our model is inspired by classical studies of the filamentation instability in unmagnetized electron–ion plasmas (Kaw et al. 1973; Max 1976). We argue that the system reaches a steady state where the ponderomotive force produced by the spatial modulations of the radiation intensity is balanced by the plasma pressure. In such a steady state, particles are confined in periodically spaced thin sheets located where the radiation intensity nearly vanishes. Electromagnetic waves propagate between the sheets as in a waveguide.

The confinement of the particles in thin sheets has important implications for FRBs. (i) The dispersion relation of electromagnetic waves resembles that in the initial homogeneous plasma, but the effective plasma frequency is determined by the separation of the sheets. (ii) The contribution of the magnetar wind to the dispersion measure of FRBs could be much larger than previously thought. (iii) The rate of induced Compton scattering is suppressed.

The paper is organized as follows. In Section 2, we review the properties of FRBs propagating in magnetar winds. In Section 3, we study the saturation of the filamentation instability in magnetized pair plasmas. In Section 4, we discuss the implications of our results for FRBs. In Section 5, we conclude.

2. FRBs in Magnetar Winds

2.1. Mean Particle Density

Magnetic field lines anchored to the magnetar surface open at the light cylinder, forming an electron–positron wind at radii $R \gtrsim R_{\rm LC} = cP/2\pi$ (P is the magnetar rotational period). For a quiescent magnetar, one can estimate the particle outflow rate as $\dot{N} \sim 10^{39}\ {\rm s}^{-1}$ and the wind bulk Lorentz factor as $\gamma_{\rm w} \sim 10^2$ (Beloborodov 2020). An actively flaring magnetar is likely to produce a denser wind with a Lorentz factor as low as $\gamma_{\rm w} \sim 10$. We will keep track of how these parameters enter the final results.

The particle number density in the wind proper frame, $n_0 = \dot{N}/4\pi\gamma_{\rm w}R^2c$, is

$$n_0 = 3 \times 10^{-3}\, \dot{N}_{39}\gamma_2^{-1}R_{14}^{-2}\ {\rm cm}^{-3}, \quad (1)$$

[7] Filamentation of strong electromagnetic waves propagating in electron–ion plasmas has been extensively studied in the field of laser plasma interaction (e.g., Kruer 2019). Filamentation has been observed in numerical simulations of relativistic magnetized shocks, in which case a strong electromagnetic precursor is emitted upstream (Iwamoto et al. 2017, 2022; Babul & Sironi 2020; Sironi et al. 2021).

where $\gamma_2 \equiv \gamma_w/10^2$, $\dot{N}_{39} \equiv \dot{N}/10^{39}\,\mathrm{s}^{-1}$, and $R_{14} \equiv R/10^{14}\,\mathrm{cm}$. The ratio of the plasma frequency, $\omega_P = \sqrt{4\pi n_0 e^2/m}$, and the FRB wave frequency in the wind frame, $\omega_0 = \pi\nu_{0,\mathrm{obs}}/\gamma_w$, is

$$\frac{\omega_P}{\omega_0} = 9 \times 10^{-5}\dot{N}_{39}^{1/2}\gamma_2^{1/2}\nu_9^{-1}R_{14}^{-1}, \tag{2}$$

where $\nu_9 \equiv \nu_{0,\mathrm{obs}}/1\,\mathrm{GHz}$ is the characteristic observed frequency in gigahertz.

2.2. Mean Temperature

Observations of weak FRBs from the Galactic magnetar SGR 1935+2154 show that radio bursts are accompanied by powerful X-ray flares (Bochenek et al. 2020; CHIME/FRB Collaboration 2020; Mereghetti et al. 2020). The isotropic equivalent of the observed luminosity is $L_r \sim 10^{37}\,\mathrm{erg\,s}^{-1}$ for the radio and $\mathcal{L}_x \sim 10^{40}\,\mathrm{erg\,s}^{-1}$ for the X-rays. Cosmological FRBs have larger radio luminosities, $L_r \sim 10^{42}\,\mathrm{erg\,s}^{-1}$. However, X-ray flares from cosmological FRBs could hardly be detected because of the enormous distance. Below, we assume that the ratio of the radio to X-ray luminosities is the same as for the Galactic magnetar SGR 1935+2154, which gives $\mathcal{L}_x \sim 10^{45}\,\mathrm{erg\,s}^{-1}$.

The electron temperature in the wind proper frame, T_0, is controlled by adiabatic expansion and Compton heating from X-rays emitted by the magnetar.[8] One may write

$$\frac{dT_0}{dR} = \left(\frac{dT_0}{dR}\right)_{\mathrm{ad}} + \left(\frac{dT_0}{dR}\right)_{\mathrm{C}}, \tag{3}$$

where the first term on the right-hand side describes adiabatic cooling, and the second term describes Compton heating.

In magnetized plasmas, the thermal velocity in the direction parallel to the local magnetic field could be different than in the perpendicular direction. The filamentation instability is independent of the thermal velocity in the perpendicular direction because particles move along the magnetic field lines as the density modulations are formed. Since the thermal velocity along the magnetic field is inversely proportional to the radius as the plasma expands (Chew et al. 1956), one may write

$$\left(\frac{dT_0}{dR}\right)_{\mathrm{ad}} = -2\frac{T_0}{R}. \tag{4}$$

The Compton heating rate of the electrons in the magnetar wind by the X-rays emitted near the surface is

$$\left(\frac{dT_0}{dR}\right)_{\mathrm{C}} = \frac{1}{\gamma_w c}\dot{N}_x\Delta T_0, \tag{5}$$

where

$$\dot{N}_x = \frac{\sigma_T\mathcal{L}_x}{4\pi R^2\gamma_w\varepsilon_x} \tag{6}$$

is the scattering rate of the X-ray photons by an electron measured in the wind proper frame (ε_x is the typical X-ray photon energy in the observer's frame), and

$$k_B\Delta T_0 = \frac{\varepsilon_x}{2\gamma_w mc^2}\left(\frac{\varepsilon_x}{2\gamma_w} - 4k_BT_0\right) \tag{7}$$

is the energy gained by the electron in one scattering (Rybicki & Lightman 1979).

Using Equations (4)–(7), Equation (3) can be presented as

$$\frac{dT_0}{dR} = -2\frac{T_0}{R} - 2\left(\frac{R_{\mathrm{cr}}}{R}\right)\frac{T_0}{R} + \frac{1}{4}\left(\frac{R_{\mathrm{cr}}}{R}\right)\frac{\varepsilon_x}{k_B\gamma_w R}, \tag{8}$$

where

$$R_{\mathrm{cr}} = \frac{\sigma_T\mathcal{L}_x}{4\pi\gamma_w^3 mc^3}. \tag{9}$$

At radii $R \ll R_{\mathrm{cr}}$, the second and third terms on the right-hand side of Equation (8) are much larger than the other terms. Then Compton scattering maintains the equilibrium of the radiation and electron temperatures, and one finds $k_BT_0 = \varepsilon_x/8\gamma_w$. At radii $R \gg R_{\mathrm{cr}}$, the first term on the right-hand side of Equation (8) is much larger than the second term. Taking into account the effect of electron recoil, one finds the solution $k_BT_0 = (\varepsilon_x/4\gamma_w)(R_{\mathrm{cr}}/R)$. The plasma is hotter than for a pure adiabatic expansion, which would give $T_0 \propto R^{-2}$. The solution of Equation (8) can be finally approximated as

$$k_BT_0 = \begin{cases} \dfrac{\varepsilon_x}{8\gamma_w} & \text{for} \quad R \ll R_{\mathrm{cr}} \\ \left(\dfrac{R_{\mathrm{cr}}}{R}\right)\dfrac{\varepsilon_x}{4\gamma_w} & \text{for} \quad R \gg R_{\mathrm{cr}}. \end{cases} \tag{10}$$

At large radii $R \gg R_{\mathrm{cr}} = 2 \times 10^9\mathcal{L}_{45}\gamma_2^{-3}\,\mathrm{cm}$, one finds

$$\frac{k_BT_0}{mc^2} = 10^{-8}\mathcal{L}_{45}\varepsilon_5\gamma_2^{-4}R_{14}^{-1}, \tag{11}$$

where $\mathcal{L}_{45} \equiv \mathcal{L}_x/10^{45}\,\mathrm{erg\,s}^{-1}$, and $\varepsilon_5 \equiv \varepsilon_x/100\,\mathrm{keV}$.

2.3. Strength Parameter of the FRB Wave

The plasma density and temperature are strongly modified with respect to the mean values of Equations (1) and (11) as a result of the filamentation instability. The instability occurs because the electrons oscillate with large velocities in the electromagnetic field of the FRB wave that propagates through the wind.

The peak velocity of an electron oscillating in the electromagnetic field of the wave is a_0c for $a_0 \ll 1$ and becomes ultrarelativistic for $a_0 \gg 1$, where the wave strength parameter is defined as $a_0 = eE_0/\omega_0 mc$. The peak electric field of the wave in the wind frame, E_0, can be calculated from the isotropic equivalent of the observed radio luminosity, $L_r = 2c\gamma_w^2E_0^2R^2$. The angular frequency of the wave in the wind frame is $\omega_0 = \pi\nu_{\mathrm{obs}}/\gamma_w$, where ν_{obs} is the observed frequency. One finds

$$a_0 = 0.2\,L_{42}^{1/2}\nu_9^{-1}R_{14}^{-1}, \tag{12}$$

where $L_{42} \equiv L_r/10^{42}\,\mathrm{erg\,s}^{-1}$.

Below, we consider the regime of large wave frequencies, $\omega_0 \gg \omega_P/a_0$. We restrict our study to the regime of nonrelativistic electron velocities ($a_0 \ll 1$ and $k_BT_0/mc^2 \ll 1$), as appropriate for radii $R \gtrsim 10^{14}\,\mathrm{cm}$.

[8] We neglect other potential sources of heating, such as magnetic reconnection (e.g., Lyubarsky & Kirk 2001) and internal shocks (e.g., Beloborodov 2020). If these processes were energetically important, our final estimate of the wind temperature, Equation (11), would be rather a lower limit. Moreover, the plasma pressure could become dominated by nonthermal particles. Then the particle velocity distribution would not be described by a nonrelativistic Maxwellian.

3. Filamentation of Strong Waves

3.1. Wave Equation

We consider an electromagnetic wave propagating in the z direction through a magnetized pair plasma. We focus on the case when the background magnetic field is transverse to the wave propagation (we set it to be in the x direction), as appropriate in magnetar winds, where the wave propagates radially and the background magnetic field is nearly azimuthal.

We look for a steady state, where the large-scale modulations of the radiation intensity are independent of time. Such a steady state can be achieved, as the e-folding time of the filamentation instability is $\sim$100 times shorter than the duration of the millisecond radio pulse (Sobacchi et al. 2022). Since planes of constant radiation intensity are perpendicular to the direction of the background magnetic field, the electromagnetic vector potential can be written as

$$A(x,\,t) = \frac{mc^2}{e} a(x) \int dk_z \hat{f}\,(k_z) \exp\left[i(k_z z - \omega t)\right], \tag{13}$$

where $\hat{f}\,(k_z)$ is peaked about the wavenumber $k_z = k_0$, and $a(x)$ describes modulations of the radiation intensity on scales $\gg k_0^{-1}$. Neglecting relativistic corrections to the electron mass, as appropriate in the limit $a_0 \ll 1$, the wave equation can be written as

$$\frac{\partial^2 A}{\partial t^2} - c^2 \nabla^2 A + \omega_{\rm P}^2 \frac{n}{n_0} A \;=\; 0, \tag{14}$$

where $\omega_{\rm P} = \sqrt{4\pi n_0 e^2/m}$ is the mean plasma frequency, and $n(x)$ is the perturbed particle density. Substituting Equation (13) into Equation (14), for a given Fourier mode, one finds

$$\frac{d^2 a}{dx^2} + \left(\frac{\omega^2}{c^2} - k_z^2 - \frac{\omega_{\rm P}^2}{c^2}\frac{n}{n_0}\right) a = 0. \tag{15}$$

In the next section, we express n/n_0 as a function of a. Then we solve Equation (15) and find the dispersion relation $\omega(k_z)$.

3.2. Particle Density

We assume that electrons and positrons have a Maxwell–Boltzmann distribution with pressure $p_0 (n/n_0)^{\Gamma}$, where $p_0 = k_{\rm B} n_0 T_0$ is the mean pressure, and Γ is the adiabatic index. Assuming that the particles move in one dimension along the strong background magnetic field lines, one finds $\Gamma = 3$.

The filamentation instability saturates when the plasma pressure balances the ponderomotive force (Kaw et al. 1973; Max 1976), namely,

$$\frac{\Gamma}{\Gamma - 1} k_{\rm B} T_0 \nabla \left(\frac{n}{n_0}\right)^{\Gamma - 1} + \nabla \phi = 0, \tag{16}$$

where $\phi = e^2 \langle A^2 \rangle / 4mc^2$ is the ponderomotive potential. The time average, $\langle \ldots \rangle$, is taken on timescales $\gg \omega_0^{-1}$ (Chen 1974). Substituting Equation (13) into the definition of ϕ and choosing the arbitrary normalization of the function $\hat{f}$ so that $\int |\hat{f}\,(k_z)|^2 dk_z = 1$, one finds

$$\phi = \frac{1}{4} mc^2 a^2. \tag{17}$$

In cold plasmas with $\beta_{\rm s} \ll \sqrt{a_0 \omega_{\rm P}/\omega_0}$, the e-folding time of the filamentation instability is shorter than the sound-crossing time of the density filaments (Ghosh et al. 2022; Sobacchi et al. 2022). In this case, pressure equilibrium cannot be maintained while the instability develops, leading to supersonic bulk motions and possibly nonadiabatic heating. Then the plasma temperature in the core of the filaments may be enhanced with respect to our estimate in Equation (20). Numerical simulations would be required to investigate this effect.

Equation (16) should be satisfied only in the regions where $n \neq 0$, since the ponderomotive force does not have any particles to push where $n = 0$. Substituting Equation (17) into Equation (16), one finds

$$\frac{n}{n_0} = \begin{cases} \left(\dfrac{\beta_{\rm max}^2 - a^2}{\beta_{\rm s}^2}\right)^{\frac{1}{\Gamma - 1}} & \text{for} \quad a < \beta_{\rm max} \\ 0 & \text{for} \quad a > \beta_{\rm max}, \end{cases} \tag{18}$$

where

$$\beta_{\rm s} = \sqrt{\frac{4\Gamma}{\Gamma - 1}\frac{k_{\rm B} T_0}{mc^2}} \tag{19}$$

is the mean thermal velocity along the background magnetic field, and

$$\beta_{\rm max} = \left(\frac{n_{\rm max}}{n_0}\right)^{\frac{\Gamma - 1}{2}} \beta_{\rm s} \tag{20}$$

is the peak thermal velocity that is achieved for $a = 0$ (in the core of the density sheets).

3.3. Solution of the Wave Equation

Equations (15) and (18) provide a second-order differential equation for $a(x)$, which is a periodic function[9] of x. The solution is subject to two constraints (Equations (21) and (22)).

The total number of particles should be the same as in the unperturbed solution (where $n(x) = n_0$ and $a(x) = a_0$ are equal to the mean values). This condition requires

$$\frac{1}{x_0} \int_0^{x_0} n(x) dx = n_0, \tag{21}$$

where x_0 is the period of $n(x)$.

The total energy density should be the same as in the unperturbed solution. The ratio of the electromagnetic energy density, $\omega_0^2 m^2 c^2 a_0^2 / e^2$, and the particle thermal energy density, $n_0 m \beta_{\rm s}^2 c^2$, is $a_0^2 \omega_0^2 / \beta_{\rm s}^2 \omega_{\rm P}^2$. For large wave frequencies $\omega_0 \gg \omega_{\rm P}/a_0$, the energy density is dominated by the electromagnetic fields. Then the conservation of the total energy requires

$$\frac{1}{x_0} \int_0^{x_0} a^2(x) dx = a_0^2. \tag{22}$$

Below, we solve Equations (15) and (18) for a cold plasma with $\beta_{\rm s} \ll a_0$ and a hot plasma with $\beta_{\rm s} \gg a_0$.

[9] As discussed in Appendix A, there are also cavity solutions, where the radiation intensity is confined in a single slab. Cavity solutions could describe the self-focusing of a laser beam (Kaw et al. 1973; Max 1976). However, the FRB wave front is broken into a large number of filaments (rather than being focused as a whole) because the transverse size of the beam is much larger than the spatial scale of the radiation intensity modulations. In this case, periodic solutions are more relevant.

3.3.1. Cold Plasma ($\beta_s \ll a_0$)

When $\beta_s \ll a_0$, the ponderomotive potential, $\phi \sim mc^2 a_0^2$, is much larger than the thermal energy per particle, $k_B T_0 \sim mc^2 \beta_s^2$. Since in Equation (16), the ponderomotive force is balanced by the plasma pressure, the particle number density should vary on very short spatial scales. This leads to the confinement of the particles into thin sheets located where the ponderomotive force nearly vanishes.

The solution of Equation (15) can be determined as follows. Since particles are confined in thin sheets, and the particle density vanishes practically everywhere, the last term of Equation (15) can be neglected (a formal justification of our assumption is presented in Appendix B). Then Equation (15) becomes

$$\frac{d^2 a}{dx^2} + \left(\frac{\omega^2}{c^2} - k_z^2\right) a = 0. \tag{23}$$

The solution of Equation (23) can be presented as

$$a = \sqrt{2}\, a_0 \sin\left(\pi \frac{x}{x_0}\right), \tag{24}$$

where

$$\omega^2 = c^2 k_z^2 + \left(\frac{\pi c}{x_0}\right)^2. \tag{25}$$

The factor $\sqrt{2} a_0$ comes from the conservation of the total energy, Equation (22). The dispersion relation resembles that in the homogeneous plasma, with an effective plasma frequency

$$\omega_{\rm P,eff} = \frac{\pi c}{x_0}. \tag{26}$$

This result has a simple physical interpretation (Max 1976). Equation (25) is analogous to the dispersion relation of electromagnetic waves propagating in a waveguide. Since the electromagnetic fields vanish for $x = 0$ and x_0, the cutoff frequency is $\pi c / x_0$.

Particles are confined in thin sheets located where $a \sim 0$. The half-thickness of the sheets, Δx, can be determined from Equation (18), which gives $a(\Delta x) = \beta_{\rm max}$. Approximating Equation (24) for small arguments of the sine function, $a(\Delta x) \sim \sqrt{2}\pi a_0 \Delta x / x_0$, one finds

$$\frac{\Delta x}{x_0} \sim \frac{\beta_{\rm max}}{a_0}. \tag{27}$$

The conservation of the total number of particles, Equation (21), gives

$$n_{\rm max}\, \Delta x \sim n_0 x_0. \tag{28}$$

From Equations (20), (27), and (28), one finds

$$\frac{\Delta x}{x_0} \sim \frac{n_0}{n_{\rm max}} \sim \frac{\beta_{\rm max}}{a_0} \sim \left(\frac{\beta_s}{a_0}\right)^{\frac{2}{\Gamma+1}}. \tag{29}$$

The electromagnetic vector potential, $a(x)$, and the particle number density, $n(x)$, are sketched in Figure 1.

The spatial scale of the radiation intensity modulations, x_0, can be estimated as follows. Linear stability analysis shows that the unperturbed solution is unstable (Ghosh et al. 2022; Sobacchi et al. 2022). When $\sqrt{a_0 \omega_{\rm P}/\omega_0} \ll \beta_s \ll a_0$, the growth rate of filamentation is sharply peaked about

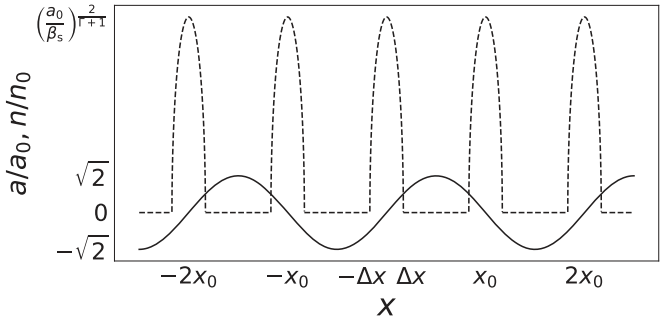

Figure 1. Sketch of the electromagnetic vector potential a (solid) and particle number density n (dashed) in the plane perpendicular to the direction of propagation of the wave. The magnetic field of the magnetar wind is directed along x. We consider a cold plasma with $\beta_s \ll a_0$ and large wave frequencies $\omega_0 \gg \omega_{\rm P}/a_0$.

$k_x = a_0 \omega_{\rm P} / 2\beta_s c$. On the other hand, when $\beta_s \ll \sqrt{a_0 \omega_{\rm P}/\omega_0}$, all of the wavenumbers $\sqrt{a_0 \omega_0 \omega_{\rm P}}/c \lesssim k_x \lesssim a_0 \omega_{\rm P}/\beta_s c$ grow at practically the same rate. Extrapolating the results of the linear stability analysis to the nonlinear stage and assuming $x_0 \sim \pi / k_x$, one finds[10]

$$x_0 \sim \frac{\beta_s c}{a_0 \omega_{\rm P}} \quad \text{for} \quad \sqrt{a_0 \omega_{\rm P}/\omega_0} \ll \beta_s \ll a_0, \tag{30}$$

$$\frac{\beta_s c}{a_0 \omega_{\rm P}} \lesssim x_0 \lesssim \frac{c}{\sqrt{a_0 \omega_0 \omega_{\rm P}}} \quad \text{for} \quad \sqrt{a_0 \omega_{\rm P}/\omega_0} \gg \beta_s. \tag{31}$$

Our results are summarized in Table 1. For large wave frequencies $\omega_0 \gg \omega_{\rm P}/a_0$, the effective plasma frequency $\omega_{\rm P,eff} = \pi c / x_0$ is much larger than $\omega_{\rm P}$.

The above estimates predict the formation of dense plasma sheets separated by near-vacuum regions. Similar structures were observed in numerical simulations of a strong electromagnetic wave propagating in a cold magnetized pair plasma (Sironi et al. 2021). The sheets were found to persist on the timescale of the simulations ($\sim 10^4/\omega_{\rm P}$).

3.3.2. Hot Plasma ($\beta_s \gg a_0$)

When $\beta_s \gg a_0$, the ponderomotive potential is much smaller than the thermal energy per particle. Then the ponderomotive force is balanced by small fluctuations of the particle density, $|n - n_0| \ll n_0$, even for large modulations of the radiation intensity.

The dispersion relation can be determined as follows. The ratio of the first and last terms of Equation (15) is $(c^2/\omega_{\rm P}^2 x_0^2)(n_0/n) \lesssim a_0^2/\beta_s^2 \ll 1$. Neglecting the first term, one finds

$$\omega^2 = c^2 k_z^2 + \omega_{\rm P}^2. \tag{32}$$

The dispersion relation is not modified by filamentation.

[10] Since a wide range of wavenumbers grow at practically the same rate when $\beta_s \ll \sqrt{a_0 \omega_{\rm P}/\omega_0}$, our argument gives only lower and upper limits of x_0. To determine the actual x_0, one should study how the instability saturates for various wavenumbers, which is outside the scope of this paper. We speculate that x_0 is determined by the power spectrum of the initial intensity fluctuations from which the instability develops. If the initial power spectrum peaks at large wavenumbers, one may have $x_0 \sim \beta_s c / a_0 \omega_{\rm P}$. If the initial power spectrum peaks at small wavenumbers, one may have $x_0 \sim c/\sqrt{a_0 \omega_0 \omega_{\rm P}}$.

Table 1
Peak Particle Number Density ($n_{\max}$), Peak Thermal Velocity ($\beta_{\max}$), Separation of the Density Sheets (x_0), Thickness of the Sheets (Δx), and Effective Plasma Frequency ($\omega_{\rm P,eff}$)

Range of $\beta_{\rm s}$	$n_{\max}/n_0$	$\beta_{\max}$	x_0	$\Delta x/x_0$	$\omega_{\rm P,eff}$
$\sqrt{a_0\omega_{\rm P}/\omega_0} \ll \beta_{\rm s} \ll a_0$	$(a_0/\beta_{\rm s})^{2/(\Gamma+1)}$	$(\beta_{\rm s}/a_0)^{2/(\Gamma+1)}a_0$	$x_0 \sim \beta_{\rm s}c/a_0\omega_{\rm P}$	$(\beta_{\rm s}/a_0)^{2/(\Gamma+1)}$	c/x_0
$\beta_{\rm s} \ll \sqrt{a_0\omega_{\rm P}/\omega_0}$			$\beta_{\rm s}c/a_0\omega_{\rm P} \lesssim x_0 \lesssim c/\sqrt{a_0\omega_0\omega_{\rm P}}$		

Note. We consider a cold plasma with $\beta_{\rm s} \ll a_0$ and large wave frequencies $\omega_0 \gg \omega_{\rm P}/a_0$. We neglect numerical factors of order unity.

4. Implications for FRBs

4.1. Effective Dispersion Measure

Below, we calculate the effective dispersion measure of FRBs propagating in magnetar winds. As discussed in Section 3, the effective plasma frequency $\omega_{\rm P,eff}$ for a cold plasma is much larger than $\omega_{\rm P}$ as an effect of filamentation. Then the dispersion measure is much larger than the value obtained for a uniform plasma density.

From Equations (25) and (26), one can calculate the group velocity of electromagnetic waves in the wind proper frame,

$$v_{\rm g} = c\sqrt{1 - \frac{\omega_{\rm P,eff}^2}{\omega^2}}. \tag{33}$$

The group velocity in the observer's frame is

$$v_{\rm g,obs} = \frac{v_{\rm g} + v_{\rm w}}{1 + v_{\rm g}v_{\rm w}/c^2}, \tag{34}$$

where $v_{\rm w}$ is the velocity of the wind. The correction to the light travel time can be presented as

$$t_{\rm w} = \int \frac{dR}{c}\left(\frac{c}{v_{\rm g,obs}} - 1\right) \simeq \frac{1}{2}\int \frac{dR}{c}\frac{\omega_{\rm P,eff}^2}{\omega_{\rm obs}^2}, \tag{35}$$

where $\omega_{\rm obs} = 2\gamma_{\rm w}\omega$ is the angular frequency in the observer's frame.

Unless magnetic reconnection or internal shocks heat the plasma well above the fiducial temperature of Equation (11), one has $\beta_{\rm s} \lesssim \sqrt{a_0\omega_{\rm P}/\omega_0}$, where ω_0 denotes the power-weighted angular frequency of the burst in the wind frame. The effective plasma frequency in the wind proper frame can be estimated from Equations (26) and (31), which give $\sqrt{a_0\omega_0\omega_{\rm P}} \lesssim \omega_{\rm P,eff} \lesssim (a_0/\beta_{\rm s})\omega_{\rm P}$. Then the contribution of the wind to the dispersion measure is $\int \left(a_0\omega_0/\omega_{\rm P}\right)n_0 dR \lesssim {\rm DM_w} \lesssim \int \left(a_0/\beta_{\rm s}\right)^2 n_0 dR$. Using Equations (1), (2), (11), and (12), one finds

$${\rm DM_{w,low}} \lesssim {\rm DM_w} \lesssim {\rm DM_{w,high}}, \tag{36}$$

where

$${\rm DM_{w,low}} = 2 \times 10^{-4}\dot{N}_{39}^{1/2}L_{42}^{1/2}\gamma_2^{-3/2}R_{14}^{-1}\ {\rm pc\ cm^{-3}}, \tag{37}$$

$${\rm DM_{w,high}} = 4 \times 10^{-2}\dot{N}_{39}L_{42}\mathcal{L}_{45}^{-1}\varepsilon_5^{-1}\gamma_2^{3}\nu_9^{-2}R_{14}^{-2}\ {\rm pc\ cm^{-3}}. \tag{38}$$

For the sake of comparison, the nominal dispersion measure of the wind (i.e., neglecting filamentation) is $\int n_0 dR = 8 \times 10^{-8}\dot{N}_{39}\gamma_2^{-1}R_{14}^{-1}$ pc cm^{-3}. Note that $\nu_9 = \nu_{0,\rm obs}/1\,{\rm GHz}$ denotes the power-weighted frequency of the burst in the observer's frame.

Equations (36) and (37) show that the contribution of the magnetar wind to the FRB dispersion measure depends on the properties of the radio burst and X-ray flare.[11] Then the dispersion measure can fluctuate significantly among different bursts from repeating FRBs. The amplitude of the fluctuations is of order ${\rm DM_w}$.

Interestingly, the dispersion measure of the bursts from the repeating FRB 20190520B fluctuates by $\sim$40 pc cm^{-3} on timescales $\lesssim$10 s. These fluctuations went unnoticed in the original paper of Dai et al. (2022) and were subsequently pointed out by Katz (2022). Fluctuations of the dispersion measure by 1–10 pc cm^{-3} on timescales $\lesssim$100 s were also reported in FRB 20121102A (Li et al. 2021) and FRB 20201124A (Xu et al. 2022), although their importance was not fully appreciated. The observed fluctuations could be produced by the magnetar wind at radii $R \sim 10^{14}$ cm. Equation (37) shows that ${\rm DM_{w,high}}$ is proportional to the particle outflow rate times the wind Lorentz factor cube, $\dot{N}\gamma_{\rm w}^3$, and to the ratio of the radio to X-ray luminosities, $L_{\rm r}/\mathcal{L}_{\rm x}$. If the wind is accelerated until the fast magnetosonic point, one finds $\dot{N}\gamma_{\rm w}^3 \sim 30\,L_{\rm w}/mc^2$, where $L_{\rm w}$ is the luminosity of the wind (Beloborodov 2020). The luminosity could be significantly larger than our fiducial value, $L_{\rm w} = 3 \times 10^{37}$ erg s^{-1}, thus increasing ${\rm DM_{w,high}}$. The ratio of the radio to X-ray luminosities could also exceed our fiducial value, $L_{\rm r}/\mathcal{L}_{\rm x} = 10^{-3}$. The FRBs from the Galactic magnetar SGR 1935+2154 were preceding the X-ray flare by $\sim$5 ms (Mereghetti et al. 2020). Then the X-ray luminosity that heats the wind during the passage of the FRB could be reduced with respect to the peak value. Taking $L_{\rm w} = 3 \times 10^{39}$ erg s^{-1} and $L_{\rm r}/\mathcal{L}_{\rm x} = 10^{-2}$, Equation (37) gives ${\rm DM_{w,high}} \sim 40$ pc cm^{-3}, consistent with the observed fluctuations of the dispersion measure of FRB 20190520B.

Another possibility is that the plasma at small radii $R \lesssim 10^{13}$ cm significantly contributes to the wind dispersion measure. However, such a contribution cannot be quantified by our estimates, which are valid only in the limit of the small wave strength parameter $a_0 \ll 1$ relevant for large radii (see Equation (12)).

4.2. Suppression of Induced Compton Scattering

Induced Compton scattering of FRBs has been discussed by several authors (for a review, see Lyubarsky 2021). Assuming the particle density and radiation intensity to be spatially uniform, the induced scattering rate can be estimated as $\Gamma_{\rm IC} \sim a_0^2\omega_{\rm P}^2/\omega_0$. However, since induced scattering grows at a slower rate with respect to filamentation when the radio burst

[11] Lu & Phinney (2020) suggested that the dispersion measure of luminous bursts may decrease due to relativistic corrections to the effective electron mass. In the magnetar wind, this effect is negligible because the inferred fluctuations of the dispersion measure are of order $\int a_0^2 n_0 dR = 10^{-9}\dot{N}_{39}L_{42}\gamma_2^{-1}\nu_9^{-2}R_{14}^{-3}$ pc cm^{-3}.

has a broad spectrum (Ghosh et al. 2022),[12] the particle density and radiation intensity are by no means uniform. The structures illustrated in Figure 1 are formed on a few e-folding times of the filamentation instability, well before induced scattering can operate.

The rate of induced Compton scattering is much smaller than the standard rate calculated for a uniform particle and radiation density. Since $\Gamma_{\rm IC} \propto a^2 n$, the scattering rate is not spatially uniform. Outside the sheets where the particles are confined, the scattering rate vanishes because $n = 0$. Inside the sheets, the particle density is $n \sim (a_0/\beta_{\rm s})^{2/(\Gamma+1)} n_0$, and the strength parameter of the wave is $a \sim (\Delta x/x_0) a_0 \sim (\beta_{\rm s}/a_0)^{2/(\Gamma+1)} a_0$ (see Equation (29)). Then the scattering rate is suppressed by a factor $(a/a_0)^2 (n/n_0) \sim (\beta_{\rm s}/a_0)^{2/(\Gamma+1)} \ll 1$.

5. Conclusions

We studied the saturation of the filamentation instability of FRBs propagating in magnetized pair plasmas. Due to the instability, the particle number density and radiation intensity are spatially modulated along the direction of the background magnetic field (assumed to be perpendicular to the direction of propagation of the wave). We find that particles are confined in periodically spaced thin sheets located where the radiation intensity nearly vanishes. Electromagnetic waves propagate between the sheets as in a waveguide. This effect has important implications.

1. The dispersion relation resembles that in the initial homogeneous plasma with an effective plasma frequency $\omega_{\rm P,eff} = \pi c/x_0$, where x_0 is the separation of the density sheets.
2. The contribution of the magnetar wind to the dispersion measure of FRBs ($\rm DM_w$) could be much larger than previously thought, possibly reaching a few tens of $\rm pc\,cm^{-3}$. Since $\rm DM_w$ depends on the properties of the radio burst and the accompanying X-ray flare, the dispersion measure can change significantly among different bursts from repeating FRBs. This effect may explain the fluctuations of the dispersion measure of the repeating FRB 20190520B.
3. The rate of induced Compton scattering is much smaller than the standard rate calculated for a uniform particle density. Outside the sheets where the particles are confined, the scattering rate vanishes because the radiation propagates in vacuum. Inside the sheets, the scattering rate is suppressed because the radiation intensity nearly vanishes.

The calculation of $\rm DM_w$ is affected by some uncertainties. (i) The properties of the magnetar wind (bulk Lorentz factor, particle outflow rate, thermal velocity dispersion) may significantly change with time as a result of the flaring activity of the magnetar. (ii) The separation of the density sheets, x_0, is uncertain. Our estimate of x_0 relies on the extrapolation of the results of the linear stability analysis of the filamentation instability. Since the linear analysis predicts that a wide range of wavenumbers grows at practically the same rate, we could only determine lower and upper limits of x_0. (iii) Our results are valid in the limit of nonrelativistic electron velocities (wave strength parameter $a_0 \ll 1$ and thermal velocity $\beta_{\rm s} \ll 1$). The contribution of the circumsource plasma (radii $R \lesssim 10^{13}$ cm, where $a_0 \gtrsim 1$) to $\rm DM_w$ should be quantified elsewhere.

[12] This is not necessarily true in electron–ion plasmas because the growth rate of the filamentation instability is lower due to the large inertia of the ions (Drake et al. 1974; Sobacchi et al. 2021). Moreover, even in a cold plasma with $\beta_{\rm s} \ll a_0$, the formation of particle sheets with a large density contrast may be hindered due to the large inertia of the ions (e.g., Schmitt & Afeyan 1998).

We thank the anonymous referee for constructive comments and suggestions that improved the paper. Y.L. acknowledges support from Israeli Science Foundation grant 2067/19. A.M. B. acknowledges support from Simons Foundation grant No. 446228, NSF AST-2009453, and NASA 21-ATP21-0056. L.S. acknowledges support from the Cottrell Scholars Award and NASA 80NSSC18K1104. M.I. acknowledges support from JSPS KAKENHI grant Nos. 20J00280 and 20KK0064.

Appendix A
Cavity Solutions

Equation (15) can be presented as

$$\frac{1}{2}\left(\frac{da}{dx}\right)^2 + V(a) = C, \tag{A1}$$

where

$$V(a) = \frac{1}{2}\left(\frac{\omega^2}{c^2} - k_z^2\right)a^2 + \frac{1}{2}\frac{\Gamma-1}{\Gamma}\beta_{\rm s}^2\frac{\omega_{\rm P}^2}{c^2}\left(\frac{n}{n_0}\right)^{\Gamma}. \tag{A2}$$

The particle number density $n(a)$ is given by Equation (18), and C is an integration constant. Equation (A1) is equivalent to the equation of motion of a particle in the potential $V(a)$.

In cavity solutions, the radiation is confined in a single slab. Such solutions are obtained when $a = da/dx = 0$ for $|x| \to \infty$ (Kaw et al. 1973; Max 1976). The conservation of the total number of particles requires $\beta_{\rm max} = \beta_{\rm s}$, so that $n = n_0$ for $|x| \to \infty$. Substituting $a = da/dx = 0$ into Equation (A1), one finds the integration constant

$$C = \frac{1}{2}\frac{\Gamma-1}{\Gamma}\beta_{\rm s}^2\frac{\omega_{\rm P}^2}{c^2}. \tag{A3}$$

The dispersion relation is determined by substituting $a = a_0$ into Equation (A1), where a_0 is the maximal value of a. Since $da/dx = 0$ for $a = a_0$, one finds

$$V(a_0) = C, \tag{A4}$$

where $V(a_0)$ and C are given by Equations (A2) and (A3). If $a_0 \gg \beta_{\rm s}$, for $a = a_0$, one finds $n = 0$. If $a_0 \ll \beta_{\rm s}$, for $a = a_0$, one finds $(n/n_0)^{\Gamma} \simeq 1 - [\Gamma/(\Gamma-1)]a_0^2/\beta_{\rm s}^2$. Then Equation (A4) gives

$$\omega^2 = c^2 k_z^2 + \omega_{\rm P,eff}^2, \tag{A5}$$

where

$$\omega_{\rm P,eff}^2 = \begin{cases} \dfrac{\Gamma-1}{\Gamma}\dfrac{\beta_{\rm s}^2}{a_0^2}\omega_{\rm P}^2 & \text{for} \quad a_0 \gg \beta_{\rm s} \\ \omega_{\rm P}^2 & \text{for} \quad a_0 \ll \beta_{\rm s}. \end{cases} \tag{A6}$$

When $a_0 \gg \beta_{\rm s}$, the effective plasma frequency is suppressed ($\omega_{\rm P,eff} \ll \omega_{\rm P}$) because in cavity solutions, the spatial scale of the region of large radiation intensity is larger than the nominal plasma skin depth $c/\omega_{\rm P}$.

Appendix B
Derivation of Equation (23)

In order to obtain Equation (23), it is sufficient to show that the second term of the potential $V(a)$ (defined in Equation (A2)) can be neglected. If $V(a_0) \gg V(0)$, the second term of $V(a)$ can be neglected because it gives a small correction to the particle velocity when $a \sim 0$.

When $a \sim a_0$, one has $n = 0$. Since $\omega^2/c^2 - k_z^2 = \pi^2/x_0^2$ (see Equation (25)), the value of the potential is $V(a_0) \sim a_0^2/x_0^2$. When $a \sim 0$, one has $n \sim (a_0/\beta_s)^{2/(\Gamma+1)} n_0$ (see Equation (29)). Then the value of the potential is $V(0) \sim \beta_s^2(\omega_P^2/c^2)(a_0/\beta_s)^{2\Gamma/(\Gamma+1)}$. The condition $V(a_0) \gg V(0)$ is satisfied for

$$x_0 \ll \left(\frac{a_0}{\beta_s}\right)^{\frac{1}{\Gamma+1}} \frac{c}{\omega_P}. \tag{B1}$$

When $\omega_0 \gg \omega_P/a_0$ and $\beta_s \ll a_0$, from Equations (30) and (31), one finds $x_0 \ll c/\omega_P$. Then Equation (B1) is satisfied.

ORCID iDs

Yuri Lyubarsky https://orcid.org/0000-0002-2316-8899
Andrei M. Beloborodov https://orcid.org/0000-0001-5660-3175
Lorenzo Sironi https://orcid.org/0000-0002-1227-2754
Masanori Iwamoto https://orcid.org/0000-0003-2255-5229

References

Babul, A.-N., & Sironi, L. 2020, MNRAS, 499, 2884
Beloborodov, A. M. 2020, ApJ, 896, 142
Bochenek, C. D., Ravi, V., Belov, K. V., et al. 2020, Natur, 587, 59
Chen, F. F. 1974, Introduction to Plasma Physics (New York: Plenum)
Chew, G. F., Goldberger, M. L., & Low, F. E. 1956, RSPSA, 236, 112
CHIME/FRB Collaboration, Andersen, B. C., Bandura, K. M., et al. 2020, Natur, 587, 54
Cordes, J. M., & Chatterjee, S. 2019, ARA&A, 57, 417
Dai, S., Feng, Y., Yang, Y. P., et al. 2022, arXiv:2203.08151
Drake, J. F., Kaw, P. K., Lee, Y. C., et al. 1974, PhFl, 17, 778
Ghosh, A., Kagan, D., Keshet, U., & Lyubarsky, Y. 2022, ApJ, 930, 106
Iwamoto, M., Amano, T., Hoshino, M., & Matsumoto, Y. 2017, ApJ, 840, 52
Iwamoto, M., Amano, T., Matsumoto, Y., Matsukiyo, S., & Hoshino, M. 2022, ApJ, 924, 108
Katz, J. I. 2022, MNRAS, 514, L27
Kaw, P., Schmidt, G., & Wilcox, T. 1973, PhFl, 16, 1522
Kruer, W. 2019, The Physics of Laser Plasma Interactions (Boca Raton, FL: CRC Press)
Li, D., Wang, P., Zhu, W. W., et al. 2021, Natur, 598, 267
Lu, W., & Phinney, E. S. 2020, MNRAS, 496, 3308
Lyubarsky, Y. 2021, Univ, 7, 56
Lyubarsky, Y., & Kirk, J. G. 2001, ApJ, 547, 437
Max, C. E. 1976, PhFl, 19, 74
Mereghetti, S., Savchenko, V., Ferrigno, C., et al. 2020, ApJL, 898, L29
Petroff, E., Hessels, J. W. T., & Lorimer, D. R. 2019, A&ARv, 27, 4
Petroff, E., Hessels, J. W. T., & Lorimer, D. R. 2022, A&ARv, 30, 2
Rybicki, G. B., & Lightman, A. P. 1979, Radiative Processes in Astrophysics (New York: Wiley)
Schmitt, A. J., & Afeyan, B. B. 1998, PhPl, 5, 503
Sironi, L., Plotnikov, I., Nättilä, J., & Beloborodov, A. M. 2021, PhRvL, 127, 035101
Sobacchi, E., Lyubarsky, Y., Beloborodov, A. M., & Sironi, L. 2021, MNRAS, 500, 272
Sobacchi, E., Lyubarsky, Y., Beloborodov, A. M., & Sironi, L. 2022, MNRAS, 511, 4766
Xu, H., Niu, J. R., Chen, P., et al. 2022, Natur, 609, 685